# EXPERIMENTAL STUDY ON AERODYNAMIC DRAG OF BOOMS AND BOOM MOUNTED STATIONARY ROTORS ON EVTOL AIRCRAFT

**Philemon Koh Jun Kai**
Research Assistant
pkoh012@e.ntu.edu.sg
Nanyang Technological University
Singapore

**Shawn Lim Kin Yip**
PhD Candidate
kinyipsh001@e.ntu.edu.sg
Nanyang Technological University
Singapore

**James Wang**
Professor
james.wang@ntu.edu.sg
Nanyang Technological University
Singapore

## ABSTRACT

In recent developments for electric Vertical Take-off and Landing (eVTOL) aircraft, there has been an influx of designs employing multiple stationary hover rotors mounted on longitudinal booms. Such layout is quite common among lift + cruise eVTOL configurations as shown in Figure 1. What is common among these eVTOL aircraft is their hover rotors only spins during hovering flight. As the aircraft transitions into forward flight, the hover rotors stop spinning, reducing the power required. Two-bladed propellers are commonly used for the hover rotors as the blades can be aligned parallel to the boom in forward flight to minimize drag. There is limited published research on the aerodynamic characteristics of boom mounted hover rotor configurations as they are not commonly found on conventional airplanes. Therefore, this paper examines how the longitudinal boom and boom-mounted hover rotors affects the aerodynamic performance of an aircraft. This involves the characterisation of the fundamental parameters that affects the performance and design of the booms and non-rotating hover rotors. Wind tunnel testing have been conducted to evaluate the aerodynamic performance of booms and boom-mounted hover rotors at their component level. Subsequently, additional studies such as the placement and size variation of fixed hover rotors were conducted to determine the directions to achieve an optimal configuration. Finally, experimental data are compared with analytical estimation using a component drag build up approach to provide comprehensive comparison between both experimental and analytical models. The results provide beneficial findings for eVTOL aircraft designers, researchers, and the VTOL industry to advance eVTOL designs with longitudinal booms and boom-mounted hover rotors.

## Notation

| | |
|---|---|
| $AR$ | Wing aspect ratio |
| $b$ | Wingspan [m] |
| $C_D$ | Total drag coefficient |
| $C_{D_i}$ | Induced drag coefficient |
| $C_{D_0}$ | Parasitic drag coefficient |
| $(C_{D_0})_{fp}$ | Parasitic drag coefficient using flat plate analogy |
| $(C_{D_0})_e$ | Parasitic drag coefficient using empirical formulations |
| $C_{D_{0,c}}$ | Component parasitic drag coefficient |
| $C_{D,interference}$ | Interference drag coefficient |
| $C_{f_c}$ | Flat plate skin friction drag coefficient |
| $C_L$ | Total lift coefficient based on front wing area |
| $C_L'$ | Total lift coefficient based on total wing area |
| $c_{root}$ | Wing root chord [m] |
| $c_{tip}$ | Wing tip chord [m] |
| $d_c$ | Average diameter of component [m] |
| $e$ | Oswald efficiency factor |
| $h_c$ | Maximum height of component [m] |
| $k_Q$ | Wing volume factor |
| $L_c$ | Component characteristic length [m] |
| $l_c$ | Length of component [m] |
| $L_{fw}$ | Lift fraction of front wing |
| $L_{rw}$ | Lift fraction of rear wing |
| $MAC$ | Mean aerodynamic chord [m] |
| $N_c$ | Number of components |
| $Q_{wing}$ | Wing volume [m$^3$] |
| $r_c$ | Average radius of component [m] |
| $Re_c$ | Component Reynolds number |
| $S_{wet,c}$ | Component wetted surface area [m$^2$] |
| $S_{wing,ref}$ | Projected surface area of reference wing [m$^2$] |
| $S_{frontal,c}$ | Component frontal area [m$^2$] |
| $S_{wing}$ | Projected wing area [m$^2$] |
| $S_{developed,c}$ | Developed area of component [m$^2$] |
| $\frac{t}{c}$ | Thickness to chord ratio |
| $V$ | Freestream velocity [m/s] |
| $w_c$ | Maximum width of component [m] |

## Greek

| | |
|---|---|
| $\lambda$ | Taper ratio |
| $\Phi_f$ | Component form factor |
| $\gamma$ | Kinematic viscosity |

# 1. Introduction

There is an increase in the number of eVTOL aircraft designs due to potential benefits of having low noise, high redundancy, and low carbon emission for aerial transportation within urban cities. The eVTOL aircraft also serves as a possible solution to reach the goal of a 50% net reduction of Green House Gas (GHG) emissions by 2050 as set by VISION 2050 [1]. However, the rising demand for electric vehicles has led to many complex designs with multiple electric powered hover rotors known as Distributed Electric Propulsion (DEP). DEP configurations are mostly arranged along (1) a single longitudinal boom or (2) many spanwise distributed rotors as shown in Figure 1 and Figure 2 respectively.

Though the longitudinal boom mounted rotors are constrained by the boom length and the distance between multiple wing surfaces, such configuration may have drag benefits due to the reduced exposed frontal area, thereby sparking interest for further investigation in this paper.

Furthermore, boom designs also provide additional advantages such as structural support for the airframe and to ensure sufficient moment arm lengths for rotors to be effective for attitude control during hover. It also allows rotors to be placed further away from the wings and fuselage, reducing downloads and blockage.

Figure 1: eVTOL aircraft with single long boom design, termed as longitudinal boom mounted rotors.

Figure 2: eVTOL aircraft with spanwise distributed rotors, termed as spanwise mounted rotors.

Previous works on eVTOL wing configurations includes Dikshit et al. who conducted a comparison on the aerodynamic, stability and handling qualities among four different eVTOL aircraft wing configurations: conventional wing-tail airplane, canard aircraft, flying wing and tandem wing aircraft [2]. Their paper highlights that the tandem wing configuration provides positive aerodynamic and stability benefits. However, their study does not consider any booms and fixed hover rotors.

While in a separate study, Nugroho et al. compared VTOL models of different wing and arm configurations [3]. In their study, the authors ran Computational Fluid Dynamics (CFD) simulations for various eVTOL configurations while considering the effects of the boom and rotors components. They highlighted that a twin boom design is the best overall configuration while the quad and tandem wing designs have an advantage in specific scenarios. However, their analysis lacks validation with experimental testing to compare with their numerical results.

As for experimental wind tunnel studies on the boom and rotors components, Stahl et al. conducted wind tunnel experiments to evaluate the drag reduction of hover rotor with a retracting and extending mechanism [4]. They demonstrated that the addition of aerodynamic drag due to the hover rotor can be minimized using their retracting mechanism. However, their desired model has a narrow and specific focus towards a single rotor mounted design on the boom. Moreover, a simplified cylindrical cap was used to represent the boom component.

In addition, Bacchini et al. expands on their work by carrying out wind tunnel analysis on an Unmanned Aerial vehicle (UAV) with different cases such as without boom and rotors, with fixed boom and rotors and with retractable boom and rotors [5]. Though not explicitly stated by the authors, the drag increase due to the individual components can be inferred from the presented results. It is observed that there is no aerodynamic fairing applied on the booms, and as such, may not be representative of an actual design.

Looking at the works of references [4] and [5], both analysis focus on the drag reduction with retractable hover rotors. The employed mechanisms are likely too mechanically complex to be implemented on a large passenger aircraft and the benefit of drag reduction is unlikely to outweigh the increase in structural weight. Hence, a compromise of having fixed hover rotors is necessary.

Experimental results from references [4] and [5] mainly presented on the changes in the overall drag coefficients and lift to drag ratio for the different aircraft configurations. This indicates that the analysis on the specific fundamental effects of the component drag for the boom and fixed hover rotors components are not well established, presenting a gap in boom and boom-mounted rotor studies.

Even though Stahl et al. conducted analytical drag modelling calculations for rotors based on several assumptions, their wind tunnel results revealed that there is an overestimation of drag between the methods used. Bacchini also highlighted that there is a greater contribution due to parasitic drag, but the specific individual components of parasite drag such as form or skin friction drag were not further analyzed.

Understanding the dominant drag component is paramount to undercover and narrow down the design parameters for an optimal low drag design. Hence, this paper presents the research done to evaluate relative changes in drag due to respective components; longitudinal boom and boom-mounted fixed rotors. It also covers the experiments for the placement and sizing of the rotor spinner to determine the dominant drag components for longitudinal boom mounted rotors and hence, parameters for low drag boom and rotor design. Lastly, experimental results are compared with analytical estimation using the component drag build up approach to provide comprehensive comparison between both experimental and analytical models.

## 2. Experimental Study

The examined aircraft model of interest employs a tandem wing multi-copter configuration with four fixed hover rotors aligned along two chordwise booms spanning across both wing surfaces. Two scaled down models were manufactured at the Nanyang Technological University (NTU) for wind tunnel experiments. They were sized based on blockage ratio of less than 10% while taking wall effects from wind tunnel into consideration [6], [7]. The models were manufactured in Polyethylene terephthalate glycol (PETG) material using a Fused Deposition Modelling (FDM) 3D printer and subsequently sanded smooth and painted to improve and ensure a consistent surface finishing for all tested models.

A closed-circuit wind tunnel at the NTU was used for the aerodynamic testing and measurements of the tested models, as shown in Figure 3. The aerodynamic loads are measured via an internally mounted load cell attached to the sting positioning system supplied by SIAC Pte Ltd. The pressure measurements are measured using a multi-hole multi-component pitot tube supplied by Aeroprobe Corporation. Aerodynamic loads are measured and recorded for each test case with a velocity sweep between 15 to 40 m/s. The respective specifications and parameters of the test apparatus used for the experiment are tabulated in both Table 1 and Table 2.

Prior work on the calibration and validation of the accuracy of the test apparatus was tested with a NACA 0015 airfoil profile and a typical spherical object. Furthermore, repeatability tests are conducted to assure that the experiment and set up is repeatable and consistent. Details on the abovementioned tests are attached in the Appendix section.


Figure 3: Closed circuit wind tunnel (top), sting position system and load cell (bottom) at NTU.

The recorded measurements are averaged based on three separate runs for each test case to ensure consistent results and to account for any random external variations. The measurements are used to determine the drag coefficient $C_D$, as calculated using Equation 1, where $D$ is the measured drag, $q$ is the measured dynamic pressure and $S_{fw}$ is the surface area of the frontal wing.

$$C_D = \frac{D}{qS_{fw}} \quad (1)$$

Thereafter, relative changes in the drag coefficient $\Delta C_{D_{case}}\%$ of various cases with the baseline are calculated using Equation 2, where $C_{D_{case}}$ is the magnitude of drag coefficient of the case and $C_{D_{baseline}}$ is the magnitude of drag of baseline respectively.

$$\Delta C_{D_{case}}\% = \left(\frac{C_{D_{case}}}{C_{D_{baseline}}} - 1\right) \times 100\% \quad (2)$$

Specifically for the final study on hover rotor placement test an overall drag discount is introduced to evaluate and compare the effect on the drag coefficient when the fixed hover rotors are placed in tandem along the longitudinal boom. The overall drag discount can be calculated using Equation 3, where $\Delta C_D\%_{4\ spinners}$ is the relative change in $C_D$ for four rotor spinners while $\Delta C_D\%_{2\ spinners\ middle}$ and $\Delta C_D\%_{2\ spinners\ rear}$ are the relative changes in $C_D$ of two rotor spinners on the middle and rear positions of the boom respectively.

$$Overall\ Drag\ Discount = 1 - \frac{\Delta C_D\%_{4\ spinners}}{\Delta C_D\%_{2\ spinners\ middle} + \Delta C_D\%_{2\ spinners\ rear}} \quad (3)$$

For an example, a drag discount value of 0 indicates that the relative drag for four spinners equals to the sum of relative drag of two spinners in the middle and the rear respectively.

Table 1: Wind tunnel specification and parameters.

| Instruments | NTU Wind tunnel |
|---|---|
| Test section Dimensions (m) | 0.78 (W) x 0.72 (H) x 2 (L) |
| Speed range (m/s) | 3 - 60 |
| Turbulence level | About 0.1% |
| Experiment test type | Velocity sweep |
| Test speed range (m/s) | 15 - 40 |
| Interval (m/s) | 1 |
| Recording time (s) | 10 |
| No of times tested per set | 3 |

Table 2: Load balance and positioning system specifications and parameters.

| Instruments | Range |
|---|---|
| Internal Load Balance | Lift force: 1000N (maximum)<br>Drag force: 500N (maximum)<br>Side force: 800N (maximum) |
| Sting Position System | Pitch Angle: -15˚ to 25˚<br>Roll Angle: -45˚ to 45˚<br>Yaw Angle: -40˚ to 40˚ |

A total of three experimental studies were conducted: (1) component inclusion test, (2) spinner size variation test, and (3) rotor spinner placement test. All baselines and test cases used for wind tunnel tests are shown in Table 3.

For the component inclusion test, the baseline case consists of the aircraft model without any boom or stationary propeller or fixed rotor. Subsequently, two additional models with booms and with a set of four stationary propellers were added to the baseline aircraft model to determine the relative changes in the drag coefficient from the additional components. This study aims to identify the total drag change for aircraft with booms and the fixed hover rotors.

Moving on to the second study on the spinner size variation test, the airplane model with booms was set as the baseline. Cylinders are modeled and used to represent the rotor spinners for the stationary propellers. The rotor spinners are sized based on the maximum height and chord of hover rotors used as depicted in Figure 4.

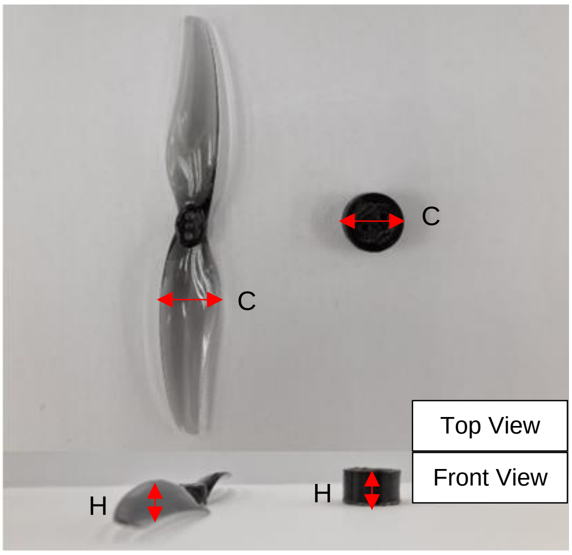


Figure 4: Sizing of rotor spinner based on hover rotor.

The baseline spinner size and dimensions are shown in Figure 4. Figure 5 shows the taller and the larger diameter spinners that were also tested. A size multiplier of three was used to amplify and exaggerate larger drag coefficient values for the experiment. The objective of the wind tunnel tests was to identify the impact of larger spinner dimensions and their impact on the eVTOL aerodynamic performance.

For the third and final study on the placement test of the fixed hover rotors, the model with booms was set as the baseline of the experiment. A pair of propeller spinners are placed along the center (two spinners middle) while in another case, a pair of rotors spinners are placed at the back of the boom (two spinners rear). Both cases are used to evaluate the relative changes in drag due to position and placement of rotor spinners. The final case is with both pairs of rotor spinners being mounted along the boom (four spinners) to determine relative changes in drag due to the number of longitudinally mounted spinners.

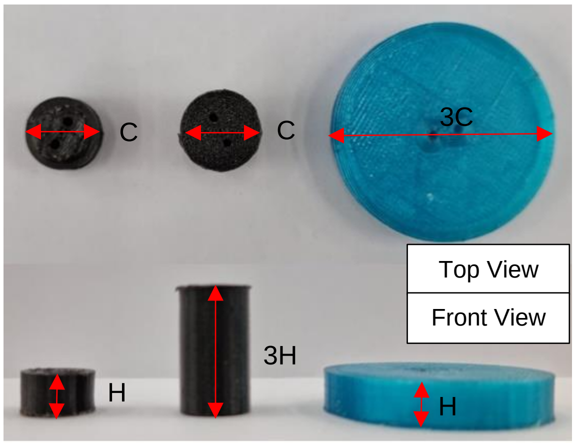


Figure 5: Standard size spinner (left), 3x taller spinner (centre), and 3x larger diameter spinner (right).

Lastly, the results are compared to baseline model with both booms and stationary rotors to determine the influence of drag from the spinners and fixed hover rotors.

Table 3: Illustration of baselines and testing configurations of all wind tunnel tests.

| Test | Testing cases | | |
|---|---|---|---|
| Components inclusion test | 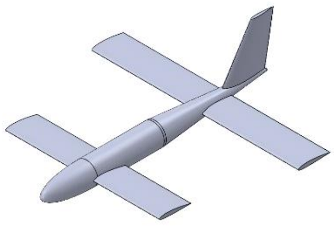 No boom | 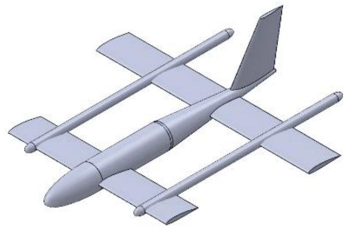 With boom | 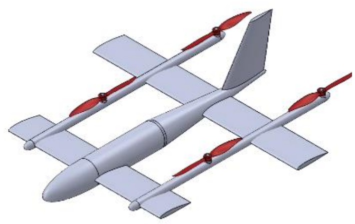 With boom and rotor |
| Spinner size variation test | 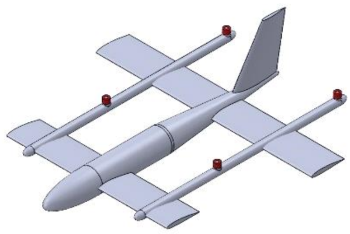 Standard spinners | 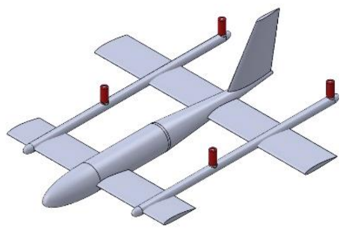 Tall spinners | 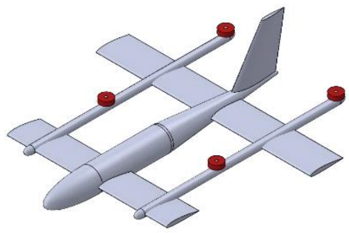 Wide spinners |
| Rotor spinner placement test | 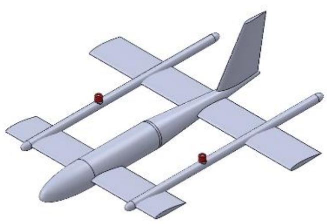 Two spinners middle | 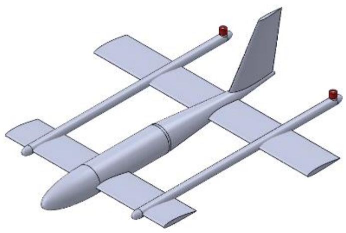 Two spinners rear | 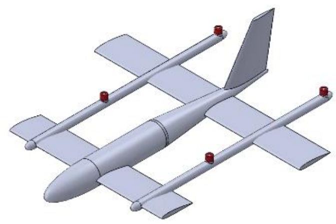 Four spinners |

# 3. Analytical Study

The objective of analytical estimation is to predict the drag of components; the longitudinal booms and boom mounted hover rotors using existing analytical equations and empirical formulations [8]. Results from analytical estimation are subsequently compared with experimental data from wind tunnel tests.

The total drag coefficient is the sum of two components as shown in Equation 4. First is the parasitic drag, $C_{D_0}$ and the second is lift induced drag $C_{D_i}$. In this formulation, it is assumed that lift induced drag for components such as longitudinal boom and stationary hover rotors are negligible as they are not considered as lift producing surfaces, therefore, lift induced drag contribution is neglected in analytical estimation. This statement will be validated in the Results and Discussion section to justify if the assumption remains valid. However, the contributions of lift induced drag may still be significant for aircraft wings as they are considered as lift generators for the aircraft. Therefore, the induced drag calculations for wings will be covered in section 3.2.2.

$$C_D = C_{D_0} + C_{D_i} \tag{4}$$

A drag build - up approach as proposed by Torenbeek is used to estimate the parasitic drag for each individual component on the aircraft [9]. The total parasitic drag $C_{D_0}$ is the combined contribution of calculated parasitic drag of selected components using the flat plate analogy $\left(C_{D_0}\right)_{fp}$, and the calculated parasitic drag for the remaining components using empirical formulations $\left(C_{D_0}\right)_e$ as shown in Equation 5. Table 4 shows the respective drag modelling method to calculate the parasitic drag for each individual component.

$$C_{D_0} = \sum \left(C_{D_0}\right)_{fp} + \sum \left(C_{D_0}\right)_e \tag{5}$$

Table 4: Modelling method used to evaluate parasitic drag of components in aircraft.

| Primary Components | Drag Modelling Method |
|---|---|
| Swept Wings<br>Fuselage<br>Booms<br>Rotor blades | Flat Plate Analogy |
| Rotor spinners<br>Interference Drag | Empirical formulation |

## 3.1. Flat Plate Analogy

The flat plate analogy is used to estimate the parasitic drag of aircraft components starting with the skin friction of a smooth flat plate with the flat surface facing parallel to the freestream turbulent air. The parasitic drag of the individual components $C_{D_{0,c}}$ can be obtained using Equation 6, where $\Phi_{f,c}$ is the form factor of the component, $C_{f_c}$ is the skin friction drag coefficient of a flat plate evaluated based on the characteristic length of the component, $S_{wet,c}$ is the wetted surface area of the component , $S_{wing,ref}$ is the projected surface area of the reference wing and $N_c$ is the number of components.

$$C_{D_{0,c}} = \frac{\Phi_{f,c} C_{f_c} S_{wet,c}}{S_{wing,ref}} \times N_c \tag{6}$$

The flat plate skin friction drag $C_{f_c}$, is determined using the empirical formula as proposed by White and Christoph in Equation 7 [10], where $Re_c$ is the Reynolds number based on the characteristic length of the respective components. Equation 7 is applicable to have a high degree of accuracy at Reynolds number between $10^5$ to $10^9$ which is slightly above the range of Reynolds number experienced in wind tunnel tests, but it is assumed to be applicable for this calculation.

$$C_{f_c} = \frac{0.42}{[\ln(0.056 Re_c)]^2} \tag{7}$$

The Reynolds number of the component $Re_c$ is calculated based on Equation 8, where $V$ is the velocity of the freestream air, $L_c$ is the characteristic length of the respective components and $\gamma$ is the kinematic viscosity of air.

$$Re_c = \frac{V L_c}{\gamma} \tag{8}$$

### 3.1.1. Wing Surfaces

Torenbeek provided an empirical chart to estimate the form factors $\Phi_f$ for both the fuselage and wings in Figure 6 [9]. For ease of calculation, the relationship between the form factors and area ratio of the frontal and wetted surface area is assumed to be linear for swept wings and fuselage, which are indicated by the blue and red lines respectively in Figure 6. It is shown that the linear assumption is valid for the fuselage but not for swept wings. However, as the sweep angle is less than 30 degrees for the wings, the linear relation for swept wing should provide a decent approximation for the swept wing. Therefore, Equations 9 and 10 were used to evaluate $\Phi_f$ for the swept wing and fuselage respectively.

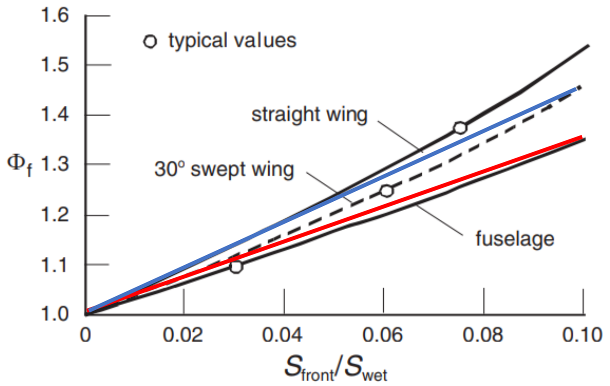


Figure 6: Empirical chart to estimate form factors by Torenbeek [9].

$$\Phi_{f,fuselage} = 3.4\left(\frac{S_{frontal,fuselage}}{S_{wet,fuselage}}\right) + 1 \qquad (9)$$

$$\Phi_{f,swept\ wing} = 5\left(\frac{S_{frontal,wing}}{S_{wet,wing}}\right) + 1 \qquad (10)$$

The frontal area of wing surface $S_{frontal,wing}$ can be approximated as shown in Equation 11, where $MAC$ is the Mean Aerodynamic Chord, $t/c$ is the thickness to chord ratio of the wing and $b$ is the span of the wing.

$$S_{frontal,wing} = MAC \times \frac{t}{c} \times b \qquad (11)$$

$MAC$ is obtained with Equation 12, where $c_{root}$ is the root chord of the wing and $\lambda$ is the taper ratio of the wing. Taper ratio is the ratio of the tip chord $c_{tip}$ and root chord $c_{root}$ as given in Equation 13.

$$MAC = \frac{2}{3} \times c_{root} \times \frac{1 + \lambda + \lambda^2}{1 + \lambda^2} \qquad (12)$$

$$\lambda = \frac{c_{tip}}{c_{root}} \qquad (13)$$

Subsequently, the wetted surface area of the wing $S_{wet,wing}$ is found using Equation 14, where $Q_{wing}$ is the volume of the wing, $AR$ is the aspect ratio of the wing and $k_Q$ is the volume factor, which is assumed to be a constant of 0.95 for tapered wings.

$Q_{wing}$ can be evaluated using Equation 15, where $S_{wing}$ is the projected surface area of the wing and $AR$ is the aspect ratio of the wing as shown in Equation 16.

$$S_{wet,wing} = \left[2 + 0.5\left(\frac{t}{c}\right)\right]\left[\frac{Q_{wing}\sqrt{AR(1+\lambda)}}{k_Q\left(\frac{t}{c}\right)}\right]^{\frac{2}{3}} \qquad (14)$$

$$Q_{wing} = \frac{k_Q\left(\frac{t}{c}\right)}{\sqrt{1+\lambda}} S_{wing}\sqrt{\frac{S_{wing}}{AR}} \qquad (15)$$

$$\text{AR} = \frac{b^2}{S_{wing}} \qquad (16)$$

Therefore, parasitic drag for wings $C_{D_{0,wing}}$ can be obtained from Equation 17. It is noted that Equations 10 to 17 are used to calculate the parasitic drag for both the front and rear wing surfaces respectively.

$$C_{D_{0,wing}} = \frac{\Phi_{f,swept\ wing} C_{f_{wing}} S_{wet,wing}}{S_{wing,ref}} \qquad (17)$$

### 3.1.2. Fuselage

Moving on to evaluate the parasitic drag for fuselage, the average diameter of fuselage $d_{fuselage}$ is approximated to be the average of the maximum height $h_{fuselage}$ and maximum width of the fuselage $w_{fuselage}$ as shown in Equation 18.

$$d_{fuselage} = \frac{1}{2}\left(h_{fuselage} + w_{fuselage}\right) \qquad (18)$$

Subsequently, the fuselage frontal surface area $S_{frontal,fuselage}$ is approximated to be a circle and can be calculated using Equation 19.

$$S_{frontal,fuselage} = \frac{\pi}{4} {d_{fuselage}}^2 \qquad (19)$$

Thereafter, the fuselage wetted surface area $S_{wet,fuselage}$ is evaluated with Equation 20, where $l_{fuselage}$ is the length of the fuselage and $1.3 \times d_{fuselage}$ is subtracted to account for taper on the nose and tail.

$$S_{wet,fuselage} = \pi d_{fuselage}\left(l_{fuselage} - 1.3 d_{fuselage}\right) \qquad (20)$$

Finally, parasitic drag for fuselage can be obtained using Equation 21 with form factor $\Phi_{f,fuselage}$ evaluated from Equation 9.

$$C_{D_{0,fuselage}} = \frac{\Phi_{f,fuselage} C_{f_{fuselage}} S_{wet,fuselage}}{S_{wing,ref}} \qquad (21)$$

## 3.1.3. Booms

The estimation of the parasitic drag for the longitudinal boom is similar to the method for the fuselage. First, the average diameter of boom $d_{boom}$ is approximated to be the average of the maximum height $h_{boom}$ and average width of the boom $w_{boom}$ given by Equation 22.

$$d_{boom} = \frac{1}{2}(h_{boom} + w_{boom}) \quad (22)$$

Subsequently, the boom frontal surface area $S_{frontal,boom}$ can be estimated using Equation 23.

$$S_{frontal,boom} = \frac{\pi}{4} {d_{boom}}^2 \quad (23)$$

Thereafter, the boom wetted surface area $S_{wet,boom}$ is evaluated with Equation 24, where $l_{boom}$ is the length of the boom.

$$S_{wet,boom} = \pi d_{boom} l_{boom} + \frac{\pi {d_{boom}}^2}{2} \quad (24)$$

Finally, parasitic drag for boom can be obtained using Equation 25 with form factor of boom approximated to be equal to $\Phi_{f,fuselage}$ evaluated from Equation 6 where $N_{boom}$ is the number of booms.

$$C_{D_{0,boom}} = \frac{\Phi_{f,fuselage} C_{f_{boom}} S_{wet,boom}}{S_{wing,ref}} \times N_{boom} \quad (25)$$

## 3.1.4. Rotor Blades

As for the parasitic drag calculation for rotor blades, the length of rotor blades $l_{blade}$ is first approximated using Equation 26 where $d_{rotor}$ is the diameter of the hover rotor and $r_{spinner}$ is the radius of rotor spinner.

$$l_{blade} = \frac{d_{rotor}}{2} - r_{spinner} \quad (26)$$

Subsequently, the total projected area or the developed area of the blades $S_{developed,blades}$ is determined with Equation 27, where $N_{rotor}$ is the number of stationary hover rotors, $N_{blades}$ is the number of blades per rotor and $c_{blade}$ is the chord of the blade. The wetted surface area is twice the developed area of blades as given in Equation 28.

$$S_{developed,blade} = N_{rotor} \cdot N_{blade} \cdot l_{blade} \cdot c_{blade} \quad (27)$$

$$S_{wet,blade} = 2S_{developed,blade} \quad (28)$$

As the thickness of blades are typically very small, hence, its frontal area $S_{frontal,blades}$ is assumed to be negligible. From Figure 6, this corresponds to a form factor $\Phi_{f,blades}$ of 1. Hence, parasitic drag for blades can be evaluated with Equation 29.

$$C_{D_{0,blade}} = \frac{C_{f_{blade}} S_{wet,blade}}{S_{wing,ref}} \quad (29)$$

## 3.2. Empirical formulation

## 3.2.1. Rotor Spinners

To evaluate the parasitic drag for the rotor spinners, cylinders ($CLD$) are used to model the rotor spinners and the frontal area of cylinder $S_{frontal,CLD}$ is determined with Equation 30, where $h_{CLD}$ is the height of cylinder and $d_{CLD}$ is the diameter of the cylinder respectively.

$$S_{frontal,CLD} = h_{CLD} \times d_{CLD} \quad (30)$$

Subsequently, parasitic drag coefficient of cylindrical spinners that is measured based on frontal area is determined from empirical charts as presented in Figure 7 [8]. It is observed that the parasitic drag is about 0.3 at Mach number below 0.2 which corresponds to the velocity range of the wind tunnel.

Therefore, parasitic drag of rotor spinners is evaluated with Equation 31, where $N_{spinner}$ is the number of spinners.

$$C_{D_{0,CLD}} = 0.3 \times \frac{S_{frontal,CLD}}{S_{wing,ref}} \times N_{spinner} \quad (31)$$

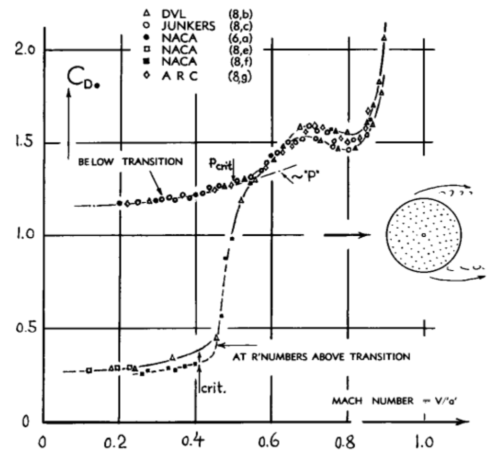


Figure 7: Empirical chart to determine parasitic drag coefficients based on frontal area [8].

## 3.2.2. Interference Drag

Empirical formula for the interference drag for wing and fuselage is determined through fitting an equation of a curve to match experimental data illustrated in Figure 8 [8]. As such, empirical formula is shown in Equation 32. As the longitudinal booms are similar to an additional fuselage, Equation 32 is assumed to be applicable for the interference drag between the wing surfaces and booms as well.

$$C_{D,interference} = \left(0.8\left(\frac{t}{c}\right)^3 - 0.0003\right) \cdot \frac{MAC^2}{S_{Wing}} \quad (32)$$

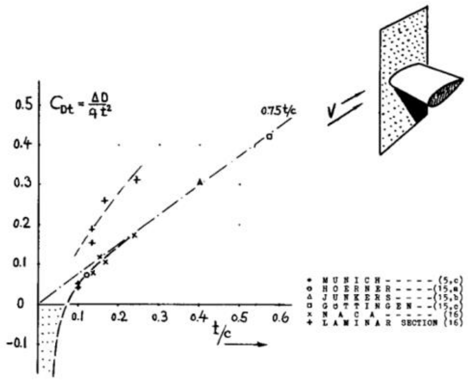

Figure 8: Empirical data for interference drag between wing and fuselage [8].

## 3.3. Lift Induced Drag for Wings

The lift coefficients for wings are taken from experimental results from the component inclusion test. As the lift coefficient is calculated based on the projected front wing area, conversion calculations are required to obtain lift coefficient based on total wing area $C_L'$ in Equation 33, where $S_{fw}$ and $S_{rw}$ are the projected areas for front and rear wing respectively.

$$C_L' = C_L \frac{S_{fw}}{S_{fw} + S_{rw}} \quad (33)$$

Subsequently, lift fractions, $L_{fw}$ and $L_{rw}$ are given to the front and rear wing respectively to estimate the lift coefficients generated from the respective wings using Equations 34 and 35. $C_{L_{fw}}$ and $C_{L_{rw}}$ are lift coefficients for both the front and rear wing respectively. $L_{fw}$ is assumed to be 0.6 while $L_{rw}$ is assumed to be 0.4 for the analysis.

$$C_{L_{fw}} = L_{fw} C_L' \quad (34)$$

$$C_{L_{rw}} = L_{rw} C_L' \quad (35)$$

Finally, the overall induced drag coefficient is determined with Equation 36, where $e$ is the Oswald efficiency factor which is assumed to be 0.75 in this calculation.

$$C_{D_i} = \frac{1}{\pi e S_{wing,ref}} \left( {C_{L_{fw}}}^2 \times S_{fw} + {C_{L_{rw}}}^2 \times S_{rw} \right) \quad (36)$$

Parasitic drag and lift induced drag from the respective components abovementioned equations are evaluated based on the dimensions of wind tunnel model aircraft. Subsequently, they are summed up to obtain the relative total drag for respective components. The result is used to validate and compare with the experimental results from wind tunnel testing in the Results and Discussion section.

# 4. Results and Discussion

## 4.1. Component inclusion test

In the first study, three cases were analyzed consisting of (1) Baseline model without boom and rotors, (2) model with booms and, (3) model with booms and fixed hover rotors. The results from components inclusion wind tunnel testing, is shown in Figure 9.

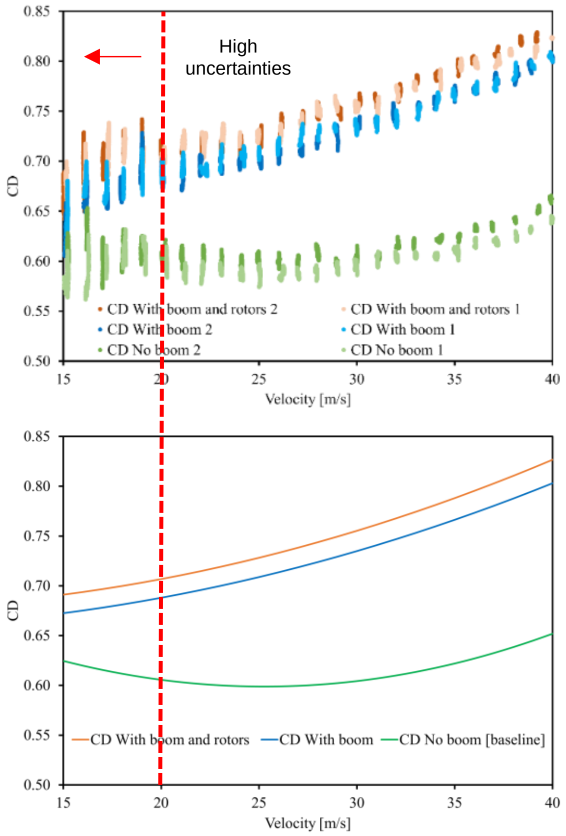


Figure 9: Variation of $C_D$ with velocity for component inclusion test. Scatterplot of raw measurements (top) and trendlines (bottom).

From the scatterplot in Figure 9, a higher uncertainty is observed at lower velocities between 15 to 20 m/s as denoted by the larger deviation values for the measured drag coefficient. This is likely due to crossflow effects in the wind tunnel being more significant at this velocity range. Hence, this region is excluded in the results evaluation.

It is observed from Table 5 that there is a significant increase in $C_D$ for the model with the longitudinal boom while there is only a smaller relative increase in $C_D$ for the model with the booms and fixed hover rotors. The large relative increase in drag from the boom component is characterized by the increase in the wetted surface area from the boom. As for the smaller relative increase in drag from the fixed rotor component, it indicates a smaller contribution of the fixed hover rotor on the drag as compared to the longitudinal booms.

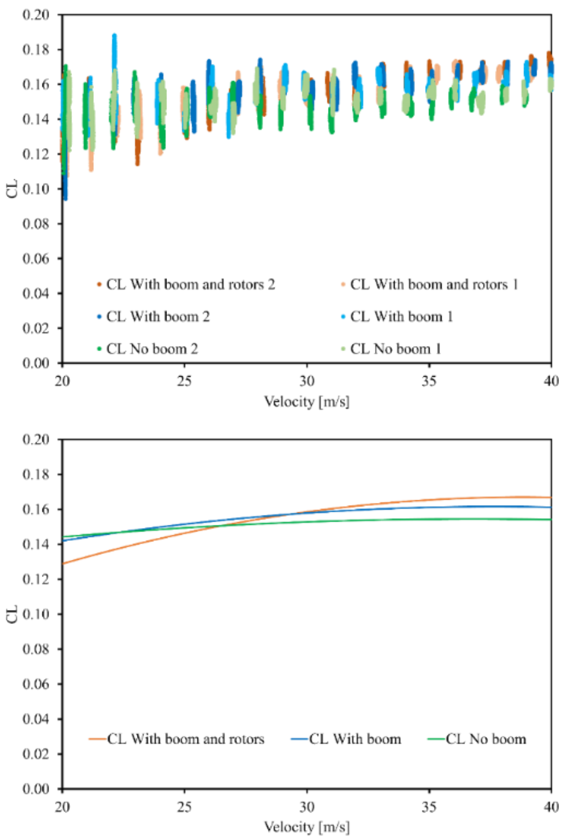


Figure 10: Variation of $C_L$ with velocity for component inclusion test. Scatterplot of raw measurements (top) and trendlines (bottom).

For the $C_L$ measurement, it shows minimal relative changes in $C_L$ for all cases as shown in Figure 10. Hence, it is unlikely that the induced drag for both the boom and fixed rotor components will contribute a significant portion of the total drag, highlighting greater influence from the parasite drag. This is in line with experimental findings from Bacchini et al. Furthermore, this also demonstrates that the assumption for negligible induced drag in the analytical estimation remains valid.

Table 5. Relative change in $C_D$% from respective components; booms and hover rotors.

| Components | $\Delta\ C_D$% |
|---|---|
| Longitudinal booms | 13.3 - 22.2 |
| Stationary hover rotors | 3.0 - 3.5 |

However, the effect of the parasitic drag component on fixed rotor cannot be determined from this experiment alone, hence, subsequent specific tests are required which led to the study of rotor spinner size variation test and subsequently, the spinner placement test.

## 4.2. Rotor spinner size variation test

In the second study, the rotor spinners sizes and dimensions are varied to determine the effect of the parasitic drag component from the different rotor spinner sizes: (1) Standard, (2) Tall and (3) Wide, as shown in Table 3. A spinner size variation test was conducted and found that $C_D$ of tall and wide spinner cases have nearly identical drag coefficients, especially at higher velocities. Therefore, as observed from both the experimental results and their parameters in Figure 11 and Table 6, the authors deduce that the main component of drag from the rotor spinners is mainly due to form drag, which is characterized by its frontal area. This is in line with the contribution of skin friction to total drag of circular cylinder plot, as shown by Heddleson et al [11].

Table 6: Parameters for rotor spinners.

| Spinner type case | Frontal area (mm$^2$) | Wetted area (mm$^2$) | Fineness ratio |
|---|---|---|---|
| Standard | 112 | 505.8 | 0.57 |
| Tall | 336 | 1209.5 | 5.14 |
| Wide | 336 | 3094.1 | 0.19 |

Therefore, this highlights that any eVTOL aircraft with rotors mounted along a single axis boom has possible benefits of reducing drag, due to the reduction of the projected frontal area, allowing for more efficient low drag design with the rotor spinner and rotor blades. However, this case study only focuses on the rotor spinners while the effects of numbers of boom mounted rotors, and their respective positions along the boom as well as the drag contributions due to rotor blades are presented in the next section.

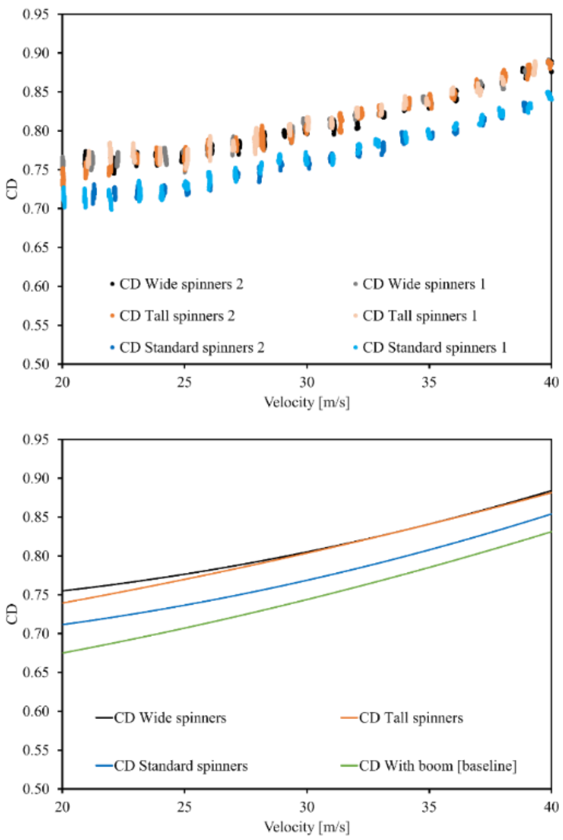


Figure 11: Variation of $C_D$ with velocity for spinner size variation test. Scatterplot of raw measurements (top) and trendlines (bottom).

## 4.3. Rotor spinner placement test

In this third and final study, the quantity and placement of rotor spinners were varied, as to study the aerodynamic effect of the position of the fixed hover rotor and drag contributions due to rotor blades. This experiment introduces four different cases, consisting of (1) with two spinners at the middle position, (2) with two spinners at the rear position, (3) with four spinners located at all positions and (4) model with booms and fixed hover rotors.

From Figure 15, it is shown that there is insignificant change in drag when switching between the two spinners at the middle position to the two spinners at the rear position. This highlights that the positioning of two spinners between the middle or rear positions has negligible impact on the overall drag coefficient.

From the previous experiment, the authors deduce the dominant drag component type for the rotor spinner is form drag as characterized by its frontal area. Since the test case of two rotor spinners in the middle and rear has the same frontal area, therefore, they should have similar form drag. This further supports the conclusion made in Rotor spinner size variation test.

When comparing the relative drag increase between the case of two spinners against the case of four spinners. A question arises from the authors: “Is the relative change in drag for four spinners less than the combined relative drag of two spinners in the middle position and the rear?” If this statement is shown to be true, this signifies that there are benefits of having a lower drag by placing hover rotors in a longitudinal boom mounted hover rotor configuration.

The question above is answered through observing the drag discount curve in Figure 14, where a positive drag discount indicates benefits of drag reduction as the sum of relative drag of two spinners at middle and rear positions respectively is larger than the relative drag of all four spinners with reference from Equation 3.

This observed drag discount is likely due to wake interactions between middle pair of rotor spinners and the rear pair as explained by Prastianto et al. [12]. The drag discount has been observed to be more prominent at lower velocities and decreases as velocity increases.

At lower velocities, it is likely that the flow across the middle pair of rotor spinners is laminar. Hence, flow likely separates at the location of maximum thickness which results in a broader turbulent wake after the middle pair of rotor spinners. This wake energizes the boundary layer on the rear pair of hover rotor spinners, which delays the flow separation and resulting in a narrower wake on the rear as shown in Figure 12. This reduces the form drag of the rear pair of rotor spinners which results in a higher drag discount [8].

However, at higher velocities, it is likely that the flow across both pairs of rotor spinners has greater energy, thereby delaying the flow separation, and reducing the wake after the middle pair of rotor spinners as shown in Figure 13. The reduction in wake size reduces wake interaction between the middle and rear pair of rotor spinners, thus reducing the drag discount. However, further verification using flow visualization or simulation is required to validate this argument.

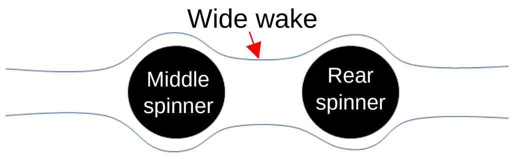


Figure 12. Wake interactions between front and rear pair of hover rotor spinners at lower velocity.

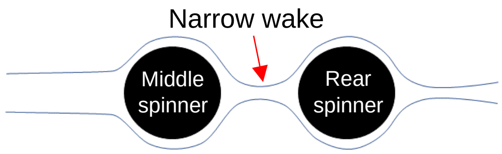


Figure 13. Wake interactions between front and rear pair of hover rotor spinners at higher velocity.

Lastly, comparing model with four spinner case with the model with four two-bladed rotors in Figure 15, it is observed that the drag contributions from rotor blades in the form of skin friction is insignificant between a selected range of velocities. However, at higher velocity, the deflections were observed from the aircraft wings and rotor blades due to the increased in lift generated at higher velocities, thus, it is likely that the increase in drag is due to form drag which is caused by an increase projected frontal area of rotor blade from the deflection.

This study shows the possible drag reduction advantages of placing fixed hover rotors along a longitudinal boom by positively manipulating the wake interactions between the middle and rear pair of hover rotors. However, at higher velocities, this benefit reduces due to the reduction in wake interaction between the middle and rear pairs of rotors, leaving the dominant drag component to be the cumulative form drag of rotor spinner and rotor blades due to deflection.

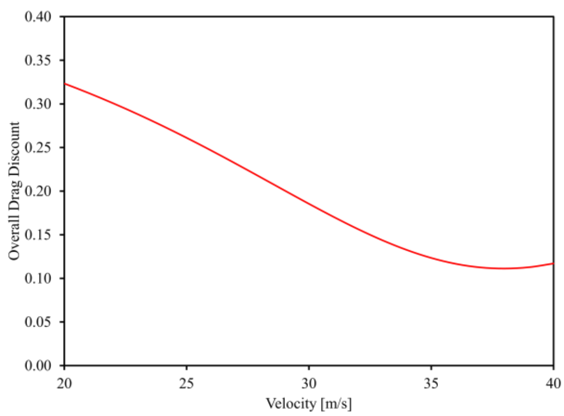


Figure 14: Drag discount curve with velocity for placement testing.

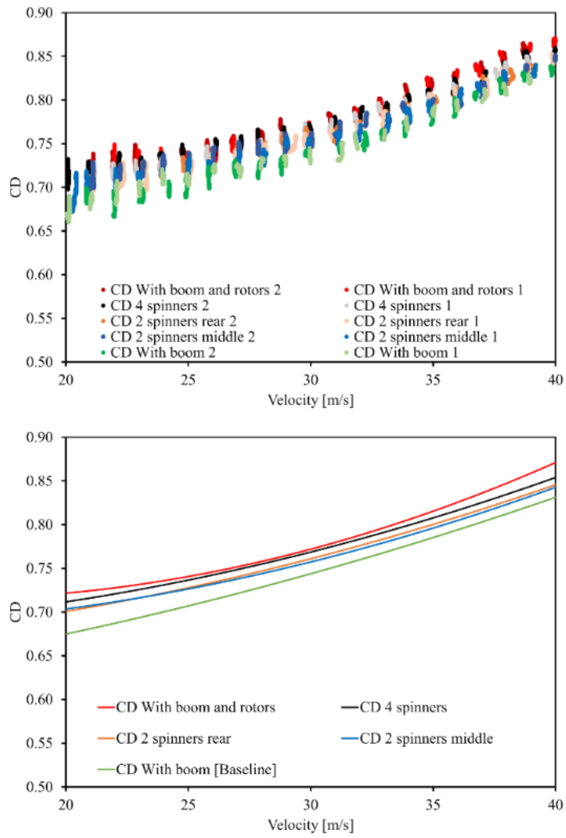


Figure 15: Variation of $C_D$ with velocity for spinner placement testing. Scatterplot of raw measurements (Top) and trendlines (Bottom).

## 4.4. Comparison Between Analytical and Experimental Results

Analytical drag estimation is modelled using drag build up method as presented by Torenbeek [9]. Details on the methodology of calculating component drag such as wings, fuselage, and booms were covered in the Analytical Study section. Subsequently, the results from analytical drag estimation are compared with experimental results from Component inclusion test for comparison which are tabulated in Table 7.

Table 7. Comparison of $\Delta\, C_D\%$ from component inclusion test and analytical estimation.

| Components | $\Delta\, C_D\%$ (Experimental) | $\Delta\, C_D\%$ (Analytical) |
|---|---|---|
| Booms | 13.3 - 22.2 | 17.4 - 17.9 |
| 4 hover rotors | 3.0 - 3.5 | 12.3 - 13.7 |

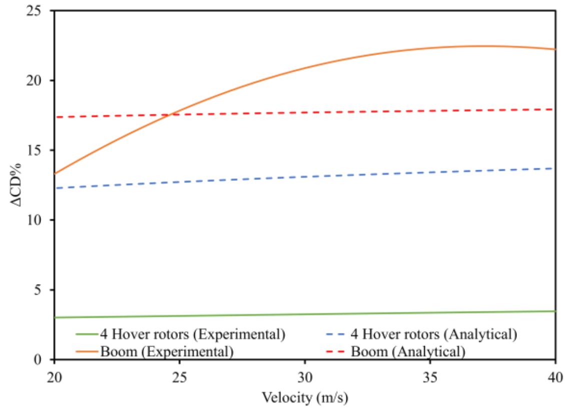


Figure 16: Variation of $\Delta\, C_D\%$ with velocity for boom and hover rotors from component inclusion test (Experimental) and analytical estimation (Analytical).

Comparing experimental values and analytical prediction for $\Delta\, C_D\%$ of the longitudinal booms in Table 7 shows good agreement with each other. However, trendlines for the experimental and analytical predictions of the longitudinal booms in Figure 16 are different in nature, that is one being non-linear and linear respectively. Therefore, analytical prediction only serves as an approximation for longitudinal boom.

Moving on to comparing analytical predictions for $\Delta\, C_D\%$ of a set of four hover rotors with the experimental results in both Table 7 and Figure 16, it shows that there is an overprediction of about four times which is observed to be relatively consistent across the entire test velocity range. This is in line with the findings from Stahl et al. where an overprediction is also observed when comparing results from the analytical drag modelling with the wind tunnel test results [4].

This is likely due to two reasons as observed from the series of wind tunnel experiments. (1) From Rotor spinner placement test, it is observed that skin friction drag due to the rotor blades is not significant from wind tunnel tests, however, they are being accounted for in the analytical estimation. (2) From Rotor spinner placement test, it is also observed that there is a positive drag discount due to wake interactions between the middle and rear pair of rotor spinners, however, the wake interactions are not being accounted for in the analytical estimation.

Therefore, the comparison between analytical predictions for $\Delta\, C_D\%$ with a set of four hover rotors and the experimental results yields a constant average fudge factor of about 0.25, which is potentially useful for subsequent analytical estimations to achieve better accuracy in modelling drag coefficient for hover rotors.

## 5. Conclusion and Future Work

The focus of this work is on understanding the drag effects of the longitudinal boom and the stationary hover rotors on eVTOL aircraft in forward flight with three aerodynamic experimental studies using wind tunnel testing.

From component inclusion test, the large increase in drag observed with the inclusion of longitudinal booms is possibly due to the large increase in **wetted surface area**, resulting in an increase in **skin friction drag**. It is also observed that lift induced drag is not likely to be the dominant drag component in booms and hover rotors.

Subsequently, rotor spinner size variation test indicates that the main component of parasitic drag for rotor spinners is **form drag**, which is characterized by its **frontal area.**

Following which, the rotor spinner placement test highlights that the position at which a pair rotor spinner is placed along the longitudinal booms have negligible changes in overall drag. Furthermore, a drag discount is given to the rear pair of rotor spinners for a set of four rotor spinners mounted on the longitudinal booms due to wake interactions between middle pair and the rear pair of rotor spinners at lower velocities. However, this discount reduces at higher velocities. Furthermore, it is also found that the skin friction drag due to propeller blades is negligible at a specified velocity range, however, deflection of rotor blades at higher velocity likely increases the projected frontal area of rotor blades, resulting in increase in form drag.

Subsequently, experimental results from component inclusion test are compared with analytical predictions using the drag build up method. It is shown that there is a good agreement for relative drag increase for booms, however, an overestimation of drag is observed for the analytical predictions of a set of four hover rotors. This is likely due to the wake interactions between the middle and rear pair of hover rotors not being considered and the skin friction drag from hover rotor blades are negligible. Therefore, empirical fudge factors are implemented to account for the abovementioned factors.

Therefore, from the series of studies, future eVTOL aircraft designs should consider **minimizing the wetted surface area** for designing a low drag longitudinal boom yet maintaining sufficient structural integrity to mount and secure the hover rotors. As for the hover rotors on an eVTOL aircraft, designs should consider **minimizing frontal area** by using **low profile rotor spinners** to reduce form drag from the hover rotors.

As this project explores the aerodynamic effects of the longitudinal booms and the boom mounted hover rotors, subsequent analysis can be expanded to spanwise mounted hover rotors to evaluate its aerodynamic effects. Thereafter, both configurations can be compared to provide valuable insights for the development of future eVTOL aircraft.

Numerical simulations can be carried out and results can be validated with the experimental results and theoretical predictions. Once numerical simulation model is robust and reliable, subsequent aircraft designs can be tested to evaluate the aerodynamic impacts in simulations. The transition from experimental testing using wind tunnel to testing in simulation offers greater time and monetary savings which allows engineers to experiment with a larger variety of eVTOL aircraft designs to determine an optimal configuration.

## 6. Acknowledgements

This research is supported by A*STAR under its MTC IAF-PP (M23L5a0019) and Nanyang Technology University grant 04INS000453C160.

## REFERENCES

[1] WBCSD, "World Business Council for Sustainable Development," 2010. Accessed: Mar. 23, 2023. [Online]. Available: https://www.wbcsd.org/contentwbc/download/1746/21728/1

[2] A. Dikshit, T. C. A. Stokkermans, S. Lim Kin Yip, and J. Wang, "Effect of Lifting Surface and Tail Configuration on the Aerodynamics and Flight Mechanics of VTOL Aircraft," in *Vertical Flight Society Forum 78*, 2022.

[3] G. Nugroho, Y. D. Hutagaol, and G. Zuliardiansyah, "Aerodynamic Performance Analysis of VTOL Arm Configurations of a VTOL Plane UAV Using a Computational Fluid Dynamics Simulation," *Drones*, vol. 6, no. 12, Dec. 2022, doi: 10.3390/drones6120392.

[4] P. Stahl, C. Rößler, and M. Hornung, "Benefit analysis and system design considerations for drag reduction of inactive hover rotors on electric fixed-wing VTOL vehicles," in *2018 Aviation Technology, Integration, and Operations Conference*, American Institute of Aeronautics and Astronautics Inc, AIAA, 2018. doi: 10.2514/6.2018-4150.

[5] A. Bacchini, E. Cestino, B. Van Magill, and D. Verstraete, "Impact of lift propeller drag on the performance of eVTOL lift+cruise aircraft," *Aerosp Sci Technol*, vol. 109, Feb. 2021, doi: 10.1016/j.ast.2020.106429.

[6] J. B. Barlow, W. H. Rae, A. Pope, and A. Pope, *Low-speed wind tunnel testing*. Wiley, 1999.

[7] A. S. M. Al-Obaidi and G. Madivaanan, "Investigation of the Blockage Correction to Improve the Accuracy of Taylor's Low-Speed Wind Tunnel," in *Journal of Physics: Conference Series*, Institute of Physics, 2022. doi: 10.1088/1742-6596/2222/1/012008.

[8] S.F.Hoerner, *Fluid-Dynamic Drag*, vol. 2. Bakersfield,CA: S.F Hoerner, 1965.

[9] E. Torenbeek, *Advanced Aircraft Design: Conceptual Design, Analysis and Optimization of Subsonic Civil Airplanes*. Netherlands: Wiley, 2013.

[10] J. D. Anderson, Aircraft performance and design. WCB/McGraw-Hill, 1999.

[11] C. F. Heddleson and D. L. Brown, "Summary of ( Drag Coefficients of (Various Shaped Cylinders," Apr. 1957.

[12] R. W. Prastianto, K. H. Dwipayana, N. Syahroni, and B. Pumbarino, "Experimental Study on Interference Effects of Two Tandem Cylinders Wrapped Around by Triple Helical Rods with Gap on Induced Drag," in IOP Conference Series: Earth and Environmental Science, Institute of Physics Publishing, Mar. 2018. doi: 10.1088/1755-1315/135/1/012025.

[13] J.M.Cimbala, "Drag on Spheres," Jan. 2012.

[14] F.A. Morrison, "Data Correlation for Drag Coefficient for Sphere," 2016. [Online]. Available: www.chem.mtu.edu/~fmorriso/DataCorrelationForSphereDrag2016.pdf.

# APPENDIX

## 1. Load cell calibration test

The objective of calibration test is to ensure the aerodynamic load measuring apparatus at NTU has good accuracy. A sphere and NACA 0015 airfoil were selected as objects of this test which is shown in Figure 17.

Figure 17: Sphere (top) and NACA0015 airfoil (bottom) used for load cell validation test.

Both specimens were chosen due to the many similar studies available, and data generated for the specimen for comparison. The manufacturing process of these objects is identical to that of aircraft models.

Sizing of sphere is done with reference to the Schlichting curve as shown in Figure 18 [13]. The maximum velocity of 40 m/s is used as the upper limit to size the sphere such that the dip in drag in the Schlichting curve is avoided. While the NACA 0015 airfoil is selected to ensure sufficient thickness for structural reinforcements.

The empirical formula for the Schlichting curve as developed by Faith A. Morrison is used as reference for drag measurements with sphere while numerical data for NACA 0015 from XFOIL is used as reference for drag measurements with airfoil [14].

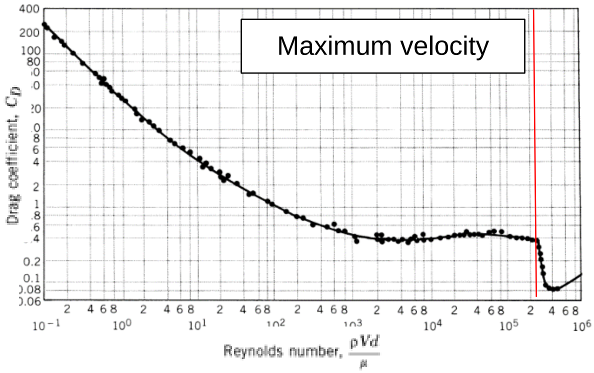


Figure 18: Schlichting curve. Experimental drag coefficient versus Reynolds number for a smooth sphere [13].

Aerodynamic drag coefficients, $C_D$ of drag data is calculated using Equation 37 for sphere and airfoil. Where, $D$ is the measured drag, $q$ is the measured dynamic pressure and $S$ is the frontal area for sphere and projected surface area for airfoil respectively. Furthermore, Equation 38 is used to determine the Reynolds number ($Re$) for load cell calibration with sphere. Where $V$ is the measured velocity, $d$ is the diameter of sphere and $\gamma$ is the kinematic viscosity of air.

$$C_D = \frac{D}{qS} \tag{37}$$

$$Re = \frac{Vd}{\gamma} \tag{38}$$

## 2. Calibration test with sphere

Comparing experimental results to that of Schlichting curve on the left graph in Figure 19, it is obvious that the dip in CD happens earlier than expected. This is likely due to manufacturing defects which increases the roughness of the sphere, hence causing flow transition to happen earlier than that of a smooth sphere. However, comparing the magnitudes between the two graphs in Figure 19, which is the drag curve for spheres with varying roughness, they are comparable to each other, hence proving that load cell measurements are relatively accurate [13].

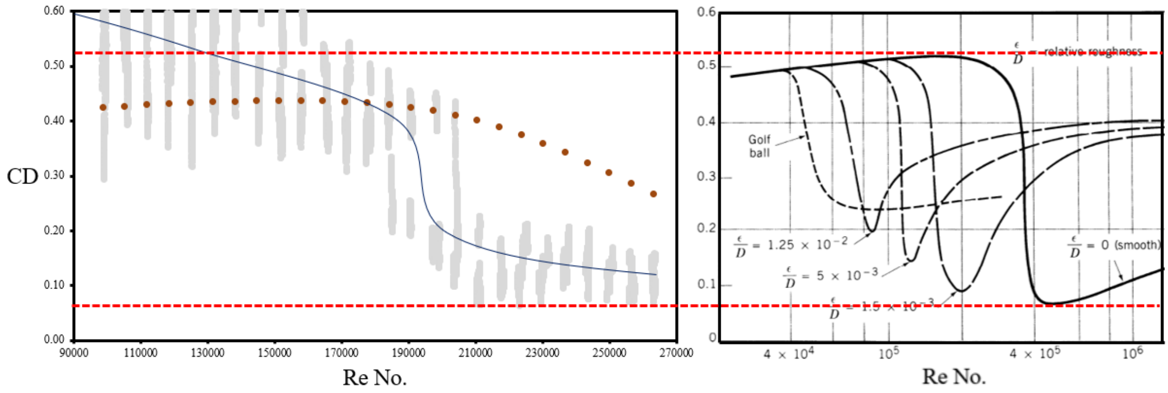


Figure 19: Comparison of experimental results with Schlichting curve (left) and drag curves of spheres with varying roughness (right).

# 3. Calibration test with NACA0015 airfoil

Results from calibration test with NACA0015 airfoil are different as compared to validation test done by sphere. A larger discrepancy is observed when comparing experimental results of NACA0015 airfoil with numerical results from XFOIL as shown in

Figure 20. Therefore, the conclusion of the calibration test is as follows: Magnitudes from experimental results are comparable to published data, however, absolute values are different. Hence, the subsequent tests with aircraft models will compare relative magnitudes instead of absolute values. Furthermore, it is difficult to achieve dynamic similarity between scaled model and full-size passenger aircraft with the current wind tunnel configuration. Hence, comparing relative magnitudes is the sensible approach to adopt.

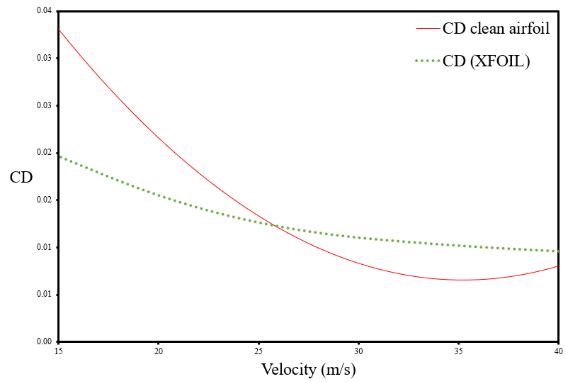


Figure 20: Comparison of experimental results of NACA0015 airfoil with numerical data from XFOIL.

# 4. Repeatability test using component inclusion test

Finally, repeatability test is carried out to ensure the current wind tunnel model setup can be repeated, hence, increasing the confidence of the measured results. Component inclusion test is performed again in a separate day and time and results shown from Figure 21 indicates that the setup is indeed repeatable.

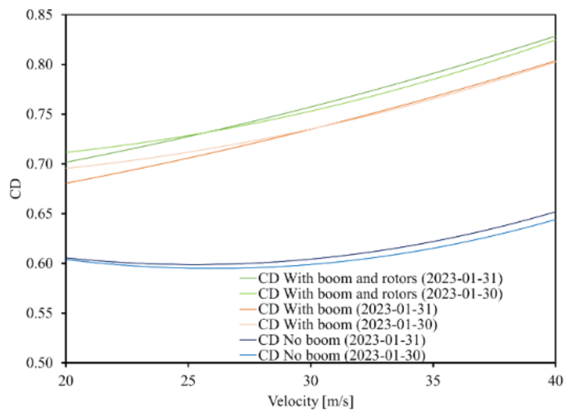


Figure 21: Component level testing is repeated in two separate day and time.